Taylor & Francis
Taylor & Francis Group

Check for updates

Experimental and Numerical Investigation of Fuel-Lean H_2/CO/Air and H_2/CH_4/Air Catalytic Microreactors

Ran Sui ⓘ, Et-touhami Es-sebbar, John Mantzaras ⓘ, and Nikolaos I. Prasianakis

Laboratory of Thermal Processes and Combustion, Paul Scherrer Institute, Villigen, Switzerland

ABSTRACT

The catalytic combustion of fuel-lean H_2/CO/air and H_2/CH_4/air mixtures (equivalence ratios φ = 0.3–0.5) was investigated experimentally and numerically in a $30 \times 30 \times 4$ mm^3 microreactor made of SiC and equipped with six 1.5-mm internal diameter platinum tubes. The goal was to demonstrate high surface temperatures (>1200 K) with good spatial uniformity, for power generation applications in conjunction with thermophotovoltaic devices. Surface temperatures were measured with an infrared camera while exhaust gas compositions were assessed with a micro gas chromatograph. Three-dimensional simulations with detailed hetero-/homogeneous chemistry, conjugate heat transfer in the solid, and external heat losses complemented the measurements. The diverse transport (Lewis number), kinetic (catalytic reactivity), and thermodynamic (volumetric heat release rate) properties of the H_2, CO, and CH_4 fuels gave rise to rich combustion phenomena. Optimization of the channel flow directions mitigated the high spatial non-uniformities of temperature, which were induced by the low Lewis number of H_2. Measured surface temperature distributions had mean values as high as 1261 K, with standard deviations as low as 10.6 K. Syngas or biogas (H_2/CO mixtures) yielded lower wall temperatures compared to undiluted H_2, even for small volumetric CO:H_2 ratios (1:9 and 2:8). Although CO had a high catalytic reactivity when combusting in H_2/CO mixtures, its larger than unity Lewis number did not allow for the attainment of high surface temperatures. Mixtures of H_2/CH_4 (such as fuels produced by natural gas decarbonization) were the least attractive due to the substantially lower catalytic reactivity of CH_4.

1. Introduction

Microreactors are of main interest for portable power generation due to their superior energy density compared to state-of-the-art Li-ion batteries (Ju and Maruta, 2011; Kaisare and Vlachos, 2012; Mantzaras, 2015). Following the latest trends in large-scale power generation for the utilization of hydrogen-containing fuels with reduced greenhouse CO_2 emissions, microreactors fueled either with hydrogen (Ghermay et al., 2010; Norton et al., 2004; Seyed–Reihani and Jackson, 2004; Sui et al., 2016) or with hydrogen-enriched hydrocarbons and syngas fuels (Federici and Vlachos, 2011; Karagiannidis and Mantzaras, 2012) have also attracted increased attention. Hydrogen can be produced

on-board from hydrocarbons using suitable microreformers (Diehm and Deutschmann, 2014; Eriksson et al., 2006; Kaisare et al., 2005; Stefanidis and Vlachos, 2009; Sui et al., 2017). The bulk of microreactors employ heterogeneous (catalytic) combustion or hybrid heterogeneous and homogeneous (gaseous) combustion concepts rather than pure gaseous combustion. This is due to the large surface-to-volume ratios of microreactors that favor catalytic surface reactions, the presence of many undesirable instabilities driven by flame-wall interactions (Evans and Kyritsis, 2009; Kurdyumov et al., 2009; Pizza et al., 2010b), and the effective suppression of these instabilities by coating the reactor surfaces with a catalyst (Pizza et al., 2009, 2010a).

High-hydrogen-content fuels at lean stoichiometries are especially challenging to combust catalytically (Mantzaras, 2014). The diffusional imbalance of hydrogen (Lewis number $Le_{H2} \sim 0.3$ at fuel-lean stoichiometries in air) leads to superadiabatic surface temperatures (Appel et al., 2002; Bui et al., 1996) that compromise the catalyst thermal stability and reactor integrity. On the other hand, for applications with desired large external heat losses (e.g., catalytic microreactors used as heat exchangers), the hydrogen superadiabaticity can be beneficial as it allows for stable combustion and at the same time for acceptably high-surface temperatures (Sui and Mantzaras, 2016).

Modern power sources should maintain a high annual capacity factor (ACF, ratio of the realized yearly output to the potential yearly output when operated at full capacity). To this direction, the European Union project Hybrid Renewable Energy Converter for Continuous and Flexible Power Production (Sui et al., 2016) investigated a combined solar/combustor microreactor with a targeted 95% ACF, operating either in sole combustion mode, sole solar mode, or combined combustion/solar mode. Catalytic microreactors operating solely with combustion have been studied in conjunction with thermoelectric, piezoelectric, and thermophotovoltaic devices for electricity production in Kyritsis et al. (2004), Kamijo et al. (2009), and Li et al. (2013). Nonetheless, optimization of the microreactor's surface temperature uniformity has not been elaborated in the past. Reported temperature differences across the investigated catalytic burners were 150 K in Kyritsis et al. (2004) and 200 K in Kamijo et al. (2009) for average reactor temperatures of ca. 1100 K.

Hydrogen-enriched fuels and biofuels are of interest in microreactors, as they can be produced from a variety of renewable sources and thus enhance the fuel supply security and flexibility. We herein extend our earlier H_2-fueled catalytic microreactor investigation (Sui et al., 2016) to the combustion of H_2/CO/air and H_2/CH_4/air mixtures at fuel-lean equivalence ratios $\varphi = 0.3$ to 0.5. The addition of CH_4 or CO to H_2 leads to rich catalytic combustion phenomena due to appreciably different thermodynamic, transport, and kinetic properties of the three fuels. CH_4 has the highest volumetric heat release rate but the lowest catalytic reactivity on Pt; H_2 has the highest reactivity on Pt, the highest molecular transport, and the lowest volumetric heat release rate; finally, CO has the lowest molecular transport and intermediate catalytic reactivity and volumetric heat release rate. Furthermore, at sufficiently low temperatures (500–600 K) there are strong kinetic interactions between H_2 and CO over Pt (Zheng et al., 2014).

Experiments are carried out at atmospheric pressure in a six-channel catalytic microreactor and involve surface temperature measurements with an infrared (IR) camera and exhaust gas analysis with a micro gas chromatograph (GC). Simulations are performed using a 3D code with conjugate heat transfer in the solid and detailed hetero-/homogeneous chemical reaction

mechanisms. Goals are to assess the fundamental catalytic combustion properties of the three individual fuel components, H_2, CO, and CH_4, at lean stoichiometries in air and to compare the microreactor performance when using $CO/H_2/air$ and $CH_4/H_2/air$ reactive mixtures in terms of attained surface temperatures and temperature spatial uniformities.

This article is organized as follows. The microreactor configuration, test-rig, and measuring techniques are presented in section 2, while the numerical methodology is described in section 3. In sections 4.1 and 4.2, fundamental properties of H_2, CO, and CH_4 catalytic combustion, which are relevant to the microreactor design, are reviewed. Comparisons between measurements and predictions are discussed in section 4.3 for the $CO/H_2/air$ and $CH_4/H_2/air$ mixtures; their combustion characteristics are further elaborated in sections 4.4 and 4.5. Conclusions are finally presented in section 5.

2. Experimental

2.1. *Catalytic microreactor*

The microreactor (Sui et al., 2016) comprises a rectangular block $30 \times 30 \times 4$ mm^3 made of SiC (see Figure 1a) with six 2.6-mm-diameter straight cylindrical channels. Six platinum tubes (99.95% purity, Wieland Edelmetalle, Germany) with 1.5-mm inner diameter (ID) and 2.5-mm outer diameter (OD) are inserted into the channels of the SiC block (Figure 1c) and the resulting 50-μm radial gaps are filled with tungsten powder (particle size ~3 μm). The tungsten powder accommodates the thermal expansion of the SiC and Pt materials and at the same time allows for efficient heat transfer between the Pt tube and the SiC block. Many such microreactors can be eventually clustered to produce a larger unit (~2 kW emitting power). The present study focuses on sole combustion mode
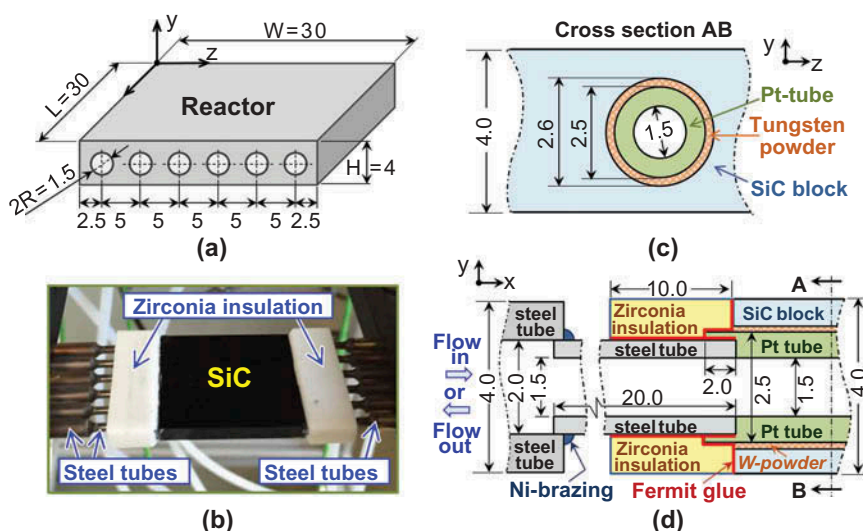
Figure 1. (a) Microreactor geometry with six channels, (b) photograph of the microreactor assembly, (c) cross-sectional view of the microreactor showing one catalytic channel, and (d) details of the catalytic channel inlet/outlet arrangement. All dimensions are in mm.

operation. In Sui et al. (2016), lean H_2/air mixtures (equivalence ratios $0.30 \leq \varphi \leq 0.50$) were used to demonstrate peak surface temperatures in excess of 1300 K with spatial non-uniformities (standard deviations of surface temperature distributions) as low as 19 K for specifically optimized channel flow configurations.

The use of solid Pt tubes instead of coating the SiC channels with a technical catalyst allows for constant surface properties (without catalyst deactivation) during long-term operation. The Pt tubes are 34 mm long, protruding 2 mm from each side of the channels (see Figure 1d), wherein the Pt tube ID is enlarged from 1.5 mm to 2.0 mm, so as to connect the Pt tubes to six high-temperature stainless steel extension tubes with an ID of 1.5 mm, OD of 2.0 mm, and length of 20 mm. These tubes are, in turn, nickel-brazed to six larger steel tubes, 4.0 mm OD and 2.0 mm ID, with a length of 100 mm (see Figure 1d) that either supply reactants to the reactor or drive the combustion products to the exhaust. The inlet and outlet faces of the reactor are insulated by two 10-mm-long zirconia blocks, while all connections are sealed with a temperature-resistant (up to 1100°C) Fermit glue to mitigate gas leakage (see Figure 1d). A photograph of the reactor assembly, zirconia insulators, and extension steel tubes is shown in Figure 1b. The effect of potential impurities (e.g., sulfuric compounds) in the fuel stream is outside the scope of this work. In any case, the trend for biogas/syngas or decarbonized natural gas is to apply a cleanup step (similar to fuel cells) that reduces such compounds to levels tolerable by the catalyst.

2.2. Test rig

A schematic of the test rig is depicted in Figure 2. High purity H_2 (99.999%), CO (99.99%), and CH_4 (99.999%) gases are supplied by pressurized bottles, while air is provided by an oil-free compressor. The total flow rates of each fuel component and air are regulated by four Brooks mass flow controllers. The fuel-to-air equivalence ratios are in the range 0.3–0.5 (accuracy ±0.7%). To ensure equal flow rates in each channel, the flows of H_2, CO, and air (or H_2, CH_4, and air) are split into six equal amounts by 3×6 dedicated ball-valve flowmeters (see Figure 2). The split flows of H_2, CO, and air (or H_2, CH_4, and air) are subsequently premixed in six 2-m-long Teflon tubes that are, in turn, connected to the six supply steel tubes of the microreactor. To facilitate catalytic ignition, external preheating of the incoming reactants is applied using two electric heating air guns; following ignition, the heating guns are removed and vigorous combustion is self-sustained.

The distribution of the reactor upper surface temperature is monitored by an infrared (IR) camera (FLIR, Type A655sc, 640×480 pixel chip), with a measuring range –40°C to 1200°C (Figure 2). The camera images the entire 30×30 mm^2 upper surface onto 125×125 pixels. The surface emissivity (required by the IR camera as an input parameter) is assessed by comparing the IR camera measurements with those of a two-color pyrometer (Maurer AG, type QKTRD1475, temperature range 400–1300°C). The two-color pyrometer is equipped with an f-300-mm objective lens and a laser-light focusing indicator, collecting radiation emitted from a circular spot ~0.2 mm^2 in size at the center of the reactor's upper surface. Pyrometer measurements consider a gray-body behavior for the emitting surface, thus canceling the effect of surface emissivity by dividing the emitted powers at two different wavelength bands (1.40–1.75 μm and 1.60–1.75 μm). The gray-
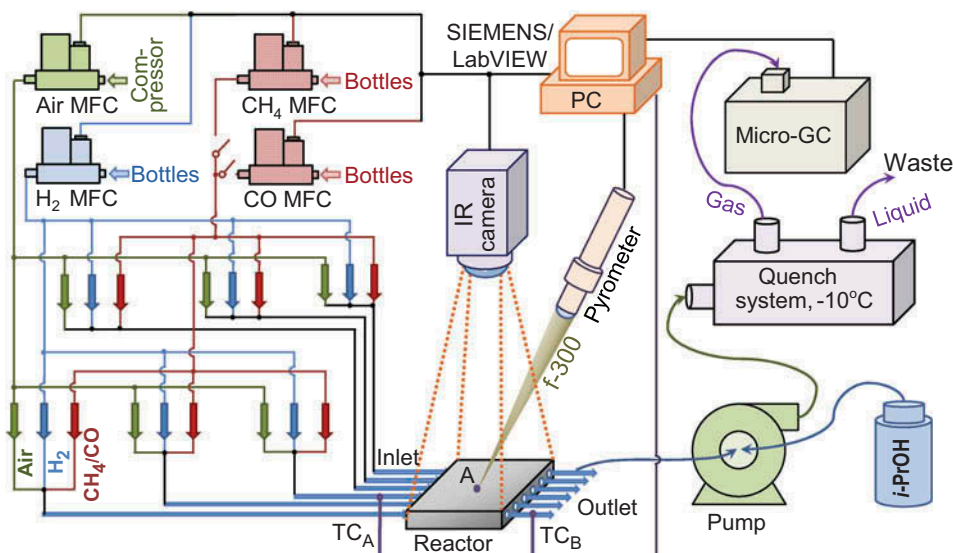
Figure 2. Schematic of the test rig with the microreactor, infrared (IR) camera, pyrometer, mass flow controllers (MFC), 3 × 6 ball flowmeters, thermocouples (TC), gas chromatograph (GC), and data acquisition system.

body emitting behavior of the SiC block (see further the natural black color of the SiC block in Figure 1b) is in turn verified independently by comparing the two-color pyrometer measurements to thermocouple measurements when the SiC block is placed in a high-temperature (400–1000°C) oven. The accuracy of the measured surface temperatures is ±25 K.

The inlet and outlet temperatures in the microreactor are monitored with several K-type sheathed thermocouples. These temperatures are used as boundary conditions in the numerical simulations. Flow rates, fuel/air equivalence ratios, surface emissivity, and temperatures are recorded by Siemens hardware and LabVIEW software. The experimental conditions are shown in Table 1. The inlet gas temperatures are 297 K with inlet velocities of 30 m/s and 50 m/s, resulting in inlet Reynolds numbers 2760–4600. The flows are still laminar due to the strong laminarization induced by the hot catalytic surfaces: it has been shown (Appel et al., 2005) that, for catalyst surface temperatures as low as 1000 K, laminar flow conditions are guaranteed even for inlet Reynolds numbers as high as 10,000.

2.3. Exhaust gas analysis

While in our foregoing H_2/air studies (Sui et al., 2016) exhaust gas composition was not measured, the two fuels in the present work necessitate the use of a GC for model validation. A GC system (CP-4900 Varian) is used for the analysis of the combustion products (Figure 2). An exhaust sample is withdrawn and injected into the GC column, using argon as a carrier gas and an automated gas valve. The sample is pumped with isopropyl alcohol (i-PrOH) into a quench system at –10°C to condense the water before entering the GC. Even though the stainless steel tubes driving the

Table 1. Experimental conditions: inlet velocity U_{IN}, equivalence ratio φ, CO:H$_2$ or CH$_4$:H$_2$ volumetric ratio, and inlet species volumetric contents with balance N$_2$.

Case	U_{IN} (m/s)	φ	CO:H$_2$/ CH$_4$:H$_2$	H$_2$ (% vol.)	CO (% vol.)	CH$_4$ (% vol.)	O$_2$ (% vol.)
A1	30	0.30	1:9	10.04	1.12	—	18.66
A2	30	0.40	1:9	12.90	1.40	—	18.00
A3	30	0.50	1:9	15.60	1.70	—	17.37
A4	50	0.30	1:9	10.04	1.12	—	18.66
A5	50	0.40	1:9	12.90	1.40	—	18.00
A6	50	0.50	1:9	15.60	1.70	—	17.37
A7	30	0.30	2:8	8.92	2.25	—	18.65
A8	30	0.40	2:8	11.47	2.89	—	17.98
A9	30	0.50	2:8	13.84	3.49	—	17.36
B1	30	0.30	1:9	7.92	—	0.89	19.15
B2	30	0.40	1:9	10.26	—	1.15	18.60
B3	30	0.50	1:9	12.47	—	1.39	18.09
B4	50	0.30	1:9	7.92	—	0.89	19.15
B5	50	0.40	1:9	10.26	—	1.15	18.60
B6	50	0.50	1:9	12.47	—	1.39	18.09
B7	30	0.30	2:8	5.82	—	1.46	19.47
B8	30	0.40	2:8	7.57	—	1.90	19.01
B9	30	0.50	2:8	9.25	—	2.32	18.57
C1	30	0.31	0.36:9.64	10.04	—	0.38	18.81
C2	30	0.41	0.35:9.65	12.90	—	0.47	18.19
C3	30	0.51	0.35:9.65	15.60	—	0.56	17.61
C4	50	0.31	0.36:9.64	10.04	—	0.38	18.81
C5	50	0.41	0.35:9.65	12.90	—	0.47	18.19
C6	50	0.51	0.35:9.65	15.60	—	0.56	17.61
C7	30	0.32	0.79:9.21	8.92	—	0.76	18.97
C8	30	0.42	0.78:9.22	11.47	—	0.97	18.39
C9	30	0.52	0.77:9.23	13.84	—	1.16	17.85

exhaust products were not cooled, there was a minimal contribution of gas-phase reactions for the present modest temperatures. This was shown with 2D simulations for a tube with a diameter of 2 mm and a length of 110 mm (the 10-mm length of the initial 1.5-mm-diameter steel tube was combined to the longer 100-mm length of the brazed 2-mm-diameter steel tubes). The gas-phase mechanisms described in the forthcoming section 3.1 were used without inclusion of catalytic chemistry. The start wall temperature ($x = 0$ mm) was taken from the reactor simulations at the end of the platinum tubes, while the end wall temperature ($x = 110$ mm) was taken from thermocouple measurements and was in the range 418–621 K. A linear wall temperature drop was imposed from the start to the end of the tube. The inlet gas compositions, inlet velocities, and inlet temperatures ($x = 0$) were again taken from the reactor simulation results at the exit of the Pt-tubes. Computed fuel conversions were minimal, as they ranged for H$_2$ and CO from 0.8% to 1.3% and for CH$_4$ from 0.7% to 0.8%.

The GC column is micropacked with a length of 0.5 m, which is sufficient for product separation. The GC system is equipped with a sensitive thermal conductivity detector for dual-channel measurements. To avoid any tailing in the peaks of the resulting chromatographs, the argon flow rate was settled at a low value of ~10 ml/min. Calibration of the GC system is accomplished using various gaseous mixtures with known compositions. The relative error in the GC measurements of the products is less than 3% for H$_2$, CH$_4$, CO$_2$, CO, and N$_2$, and up to 30% for O$_2$.

3. Numerical

The 3D modeling entails the coupling of two codes, one for the combustion in the channels and a second one for the solid heat conduction and external heat losses. The developed code has been detailed in Sui et al. (2016), where it was applied to model H_2/air combustion in the microreactor. In the following, the main code features are briefly summarized.

3.1. *Combustion modeling*

A 2D steady parabolic code simulates the channel-flow combustion (Sui et al., 2016). The parabolic model is justified given the high inlet Reynolds numbers (up to 4600 as stated in section 2.2). Uniform temperature, gas compositions, and velocity are applied at the inlets ($x = 0$). No-slip is used for both velocity components at the gas-wall interface ($r = R$), while the axial wall temperatures along the channel are supplied by the solid heat conduction code.

Detailed catalytic reaction mechanisms for simple fuels (such as H_2, CO, and CH_4) on platinum surfaces have advanced in recent years (Bui et al., 1996; Deutschmann et al., 2000; Kraus and Lindstedt, 2017). Here, the detailed catalytic reaction mechanism for H_2/ CO/CH_4 oxidation on Pt (Deutschmann et al., 2000) is employed (14 reactions, five surface and nine gaseous species). For gas-phase combustion, the H_2/CO mechanism from Li et al. (2007; 36 reactions and 13 species) and for H_2/CH_4 the C1-mechanism from Warnatz et al. (1996; 108 reactions and 25 species) are used. The employed gas-phase mechanisms have been validated in their capacity to reproduce the onset of homogeneous ignition (assessed with laser-induced fluorescence of the OH radical) in a Pt-coated channel for fuel-lean CO/H_2/air mixtures (Ghermay et al., 2011a) and for fuel-lean CH_4/air mixtures (Reinke et al., 2002).

Surface and gas-phase reaction rates are evaluated with Surface-Chemkin (Coltrin et al., 1996) and Chemkin (Kee et al., 1996b), respectively, while transport properties are calculated from the Chemkin database (Kee et al., 1996a).

3.2. *Solid heat conduction and external heat loss modeling*

The steady 3D heat conduction (including the SiC block and the Pt tubes) and the surface external heat losses are computed with the open source software OpenFOAM (OpenFOAM, 2014). It was shown in Sui et al. (2016) that, without any loss in accuracy and for the purpose of having a computationally affordable grid resolution, the 50-μm-thick tungsten powder layers could be modeled either as Pt or SiC. In the following, the tungsten powder layers were treated as SiC. The thermal conductivity of the SiC block is modeled with a fifth-order polynomial function of temperature (Sui et al., 2016); over the range 750–1300 K, which is of interest in the present study; the SiC thermal conductivity drops from 105.1 Wm^{-1} K^{-1} to 57.2 Wm^{-1} K^{-1}. The thermal conductivity of the Pt tubes is approximated by a linear function of temperature (Sui et al., 2016); over the range 750–1300 K it increases from 74.6 Wm^{-1} K^{-1} to 83.9 Wm^{-1} K^{-1}.

The solid geometry is discretized with 5.8 million tetrahedral cells having 28,000 cell surfaces on every channel, which ensure grid-independent and smooth temperature distributions. Heat losses are estimated at the entry and outlet sides of the reactor, assuming a linear temperature drop from the end faces of the SiC block through the zirconia insulators and the steel connecting tubes down to the exposed vertical faces of the zirconia insulators (10 mm length along the x-direction, see Figure 1d), with thermal conductivities for the zirconia and steel of 2 $Wm^{-1} K^{-1}$ and 26 $Wm^{-1} K^{-1}$, respectively. To this direction, temperatures are measured at the exposed vertical faces of the zirconia blocks and the steel connecting tube external surfaces (at the same axial distance) with K-type thermocouples.

At the fully exposed four surfaces, i.e., upper, lower, left, and right, natural convective and radiative heat losses are considered. The natural convective heat loss coefficients h at the outer surfaces are estimated using empirical formulas from ASHRAE (2009) for a quiescent environment: $h = 21.6$ $Wm^{-2} K^{-1}$ for the upper surface, $h = 10$ $Wm^{-2} K^{-1}$ for the lower surface, and $h = 30.7$ $Wm^{-2} K^{-1}$ for the vertical sides. For the radiative heat loss, the surface emissivity is accessed by the two-color pyrometer and IR camera and varies from 0.56 to 0.68. The emissivity exhibits a nearly linear dependence on temperature, as shown in Figure 3. Literature values of the SiC total emissivity are typically in the range of 0.80–0.95. However, the surface emissivity is a strong function of the surface finishing process, and in our case a very fine polishing has been applied (see Sui et al., 2016).

The channel combustion code and the OpenFOAM code are coupled iteratively until a converged steady state solution is achieved. The combustion code uses the channel wall temperatures as input and calculates the heat fluxes at the channel surfaces, while the OpenFOAM uses the wall heat fluxes as input parameters and computes the temperature distributions in the solid and the heat losses at the external surfaces.
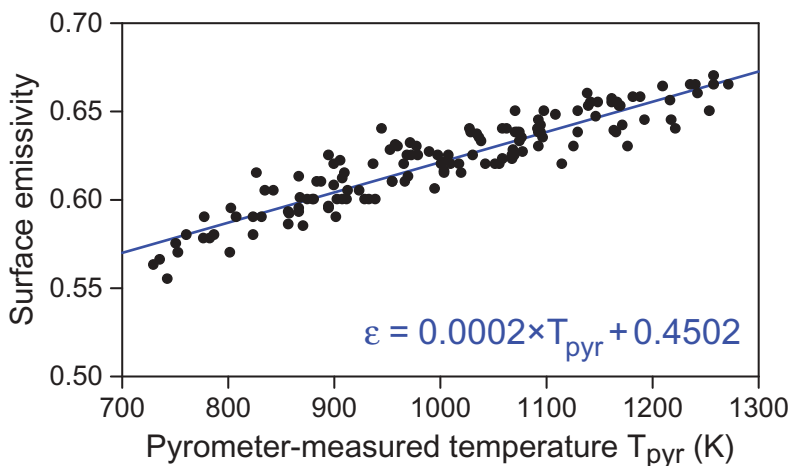
Figure 3. Measured emissivity of the microreactor top surface and linear regression as a function of pyrometer-measured surface temperature (T_{pyr}).

4. Results and discussion

Fundamental hetero-/homogeneous combustion characteristics of the three investigated fuels (H_2, CO, and CH_4) in a Pt-coated single catalytic channel are first discussed to expose the roles of transport, reactivity, and exothermicity. Experimental and numerical results for the microreactor in Figure 1 are then compared in terms of surface temperatures and exhaust gas compositions.

### 4.1. Fundamentals of H₂, CO, and CH₄ hetero-/homogeneous combustion

For deficient reactants with Lewis numbers less (greater) than unity, the catalyst surface temperatures are higher (lower) than the adiabatic equilibrium temperatures under the conditions of adiabaticity, infinitely-fast catalytic chemistry, and absence of gaseous chemistry. Specifically, the wall temperature in a channel-flow geometry attains a maximum or minimum value at the channel entry ($x \rightarrow 0$), depending on whether the Lewis number, Le, of the deficient reactant is smaller or larger than unity (see Zheng and Mantzaras, 2014):

$$\mathrm{T}_{\mathrm{w,\ max\,/\,min}} = T_{\mathrm{IN}} + Le^{-2/3}(\Delta T)_{\mathrm{c}} \tag{1}$$

where T_{IN} is the inlet temperature and $(\Delta T)_{\mathrm{c}}$ the adiabatic combustion temperature rise (= $T_{\mathrm{ad}} - T_{\mathrm{IN}}$, with T_{ad} the adiabatic equilibrium temperature of the incoming reacting mixture). The Lewis numbers of H_2, CH_4, and CO for a fuel-lean equivalence ratio of 0.3 in air are 0.35, 0.97, and 1.06, respectively (calculated using the transport package of Chemkin; Kee et al., 1996a). Equation (1) yields a maximum superadiabatic surface temperature $T_{\mathrm{w,max}} > T_{\mathrm{ad}}$ for $Le < 1$ (H_2 and CH_4) and a minimum underadiabatic temperature $T_{\mathrm{w,min}} < T_{\mathrm{ad}}$ for $Le > 1$ (CO).

To clarify this behavior, streamwise profiles of the computed wall temperatures T_{w}, mean gas temperatures $T_{\mathrm{gas-m}}$, and fuel conversions are presented in Figure 4 for a Pt-coated single tubular channel with similar geometrical characteristics as the Pt tubes in Figure 1 (1.5-mm ID, length 30 mm, but with a smaller OD of 1.6 mm). Inlet conditions refer to H_2/air ($\varphi = 0.3$, Figures 4a, a1), CO/air ($\varphi = 0.3$, Figures 4b, b1), and CH_4/air ($\varphi = 0.3$ and 0.4, Figures 4c, c1), with $T_{\mathrm{IN}} = 300$ K, $U_{\mathrm{IN}} = 15$ m/s, and $p = 1$ bar. The outer channel walls are adiabatic and the solid has a thermal conductivity equal to that of Pt (see section 3.2). A 2D Navier–Stokes reactive CFD code (Ghermay et al., 2010; Karagiannidis et al., 2011) simulates the flow and solid heat conduction with a mesh of 150×48 cells for the gas (30×0.75 mm^2) and 150×20 points for the solid (30×0.05 mm^2), which is sufficient to produce a grid-independent solution.

For each fuel, three cases are simulated. In Cases 1 (marked $T_{\mathrm{w,1}}$ and $T_{\mathrm{gas-m,1}}$) heat conduction in the solid wall is suppressed (solid thermal conductivity $\lambda_s = 0$, in order to avoid redistribution of energy along the channel) while only catalytic chemistry (C) is included (no gaseous chemistry), which is further considered to be infinitely fast (transport-limited conversion of the deficient fuel reactant). The transport-limited modeling has been elaborated in Zheng and Mantzaras (2014). Cases 2 (marked $T_{\mathrm{w,2}}$ and $T_{\mathrm{gas-m,2}}$) use the detailed catalytic (C) reaction mechanism from Deutschmann et al. (2000; again without inclusion of gaseous chemistry), while Cases 3 (marked $T_{\mathrm{w,3}}$ and $T_{\mathrm{gas-m,3}}$) refer to the detailed catalytic and gas-phase ($C + G$) mechanisms of
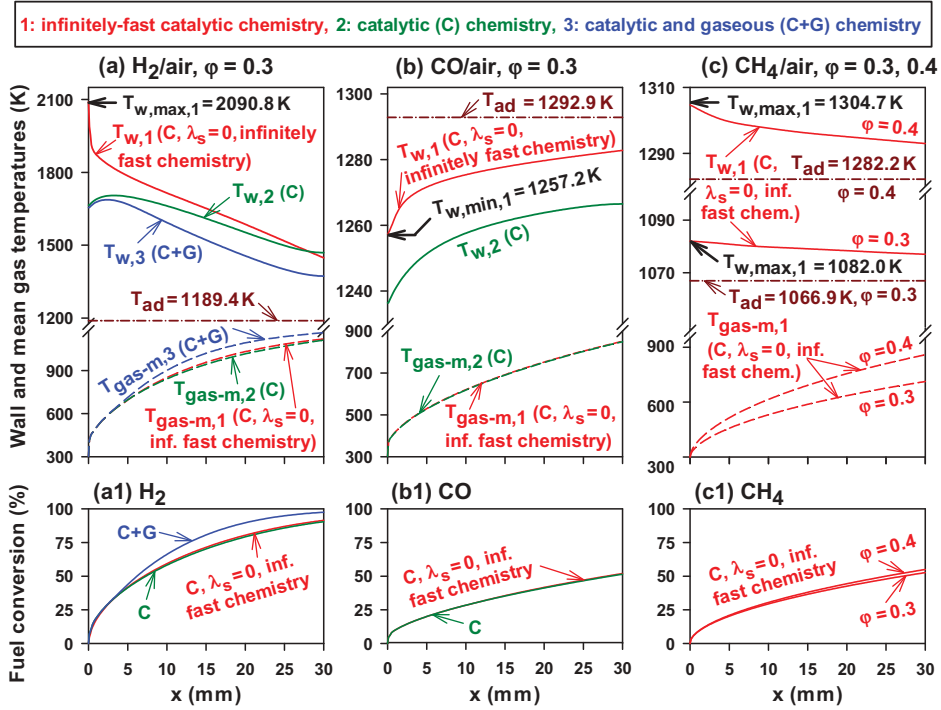
Figure 4. Computed wall temperatures (T_w, solid lines), mean gas temperatures (T_{gas-m}, dashed lines) and fuel conversions in a Pt-coated cylindrical channel with 30-mm length, 1.5-mm internal diameter, 1.6-mm external diameter, and adiabatic outer walls. The following simulations are shown: (1) infinitely fast catalytic (C) chemistry (no gaseous chemistry) and no heat conduction in the solid; (2) detailed catalytic (C) chemistry (no gaseous chemistry) with heat conduction in the solid; and (3) detailed catalytic and gas-phase (C + G) reaction mechanisms with heat conduction in the solid. (a) H_2/air, (b) CO/air, and (c) CH_4/air combustion with T_{IN} = 300 K, U_{IN} = 15 m/s, p = 1 bar. In (a) and (b), φ = 0.3 and in (c) φ = 0.3 and 0.4 are shown. The horizontal lines marked T_{ad} denote the adiabatic equilibrium temperatures of the incoming mixtures. Percent fuel conversions are shown in (a1), (b1), and (c1).

section 3.1. In addition, the models for Cases 2 and 3 include heat conduction inside the solid wall. The solid curves in Figures 4a, 4b, and 4c signify the inner wall temperatures T_w (at the gas-wall interface $r = R$): radial temperature variations inside the solid for Cases 2 and 3 are typically less than 15 K. The dashed lines are the mean gas temperatures and the horizontal dashed-dotted lines are the adiabatic equilibrium temperatures T_{ad} based on the inlet mixture properties. Finally, the maximum or minimum wall temperatures $T_{w,max}$ and $T_{w,min}$ at $x \rightarrow 0$ for Cases 1 (infinitely fast catalytic chemistry) are marked by thick arrows.

4.1.1. H_2/air catalytic combustion

Due to the significantly lower than unity Lewis number of H_2, Le_{H2} = 0.35 evaluated using the Chemkin transport package (Kee et al., 1996a), the computed $T_{w,1}$ for Case 1 in Figure 4a at the channel entry ($x = 0$) reaches a maximum value $T_{w,max,1}$ = 2090.8 K, which is 901 K higher than the adiabatic equilibrium temperature T_{ad}. This is in good

agreement with the theoretical maximum of 2099.7 K evaluated from Eq. (1). The wall temperature $T_{w,1}$ drops farther downstream and would have eventually reached T_{ad} upon complete consumption of hydrogen, which however does not occur within the 30-mm channel length.

The wall temperature $T_{w,2}$ in Figure 4a is lower than $T_{w,1}$ over most of the channel length due to the combined effects of finite-rate catalytic chemistry and redistribution of heat in the solid via conduction. Although appreciably lower than $T_{w,max,1}$, the peak value of $T_{w,2}$ = 1704.9 K is 515.5 K higher than the adiabatic equilibrium temperature. Moreover, finite rate chemistry yields up to 16 K lower mean gas temperature $T_{gas-m,2}$ compared to $T_{gas-m,1}$ and slightly lower H_2 conversion (90.4% compared to 91.5% for Case 1, see Figure 4a1).

Case 3 with both surface and gaseous chemistries yields the lowest maximum wall temperature $T_{w,3}$, which is however still above T_{ad}. $T_{w,3}$ is noticeably lower than $T_{w,2}$ over $x > 5$ mm. This is due to the suppression of surface combustion by gaseous combustion; it was shown in Ghermay et al. (2011b) that gaseous chemistry moderates the catalytically-induced surface superadiabaticity by shielding the catalyst from the H_2-rich channel core. On the other hand, $T_{gas-m,3}$ is the highest among the three cases, which is undesirable due to the higher thermal energy of the exhaust gases. Gas-phase combustion also leads to higher H_2 conversions (97.5% for Case 3, see Figure 4a1). Overall, gaseous chemistry reduces the wall temperatures ($T_{w,3}$) and also deteriorates the temperature spatial uniformity. For this reason (and also because of the higher $T_{gas-m,3}$) gas-phase combustion is avoided by proper reactor design.

4.1.2. CO/air catalytic combustion

Contrary to hydrogen, carbon monoxide has a slightly larger than unity Lewis number, leading to catalytic wall temperatures lower than the corresponding adiabatic equilibrium temperatures (Figure 4b). Case 1 in Figure 4b with infinitely fast catalytic chemistry and no solid heat conduction yields a minimum wall temperature at the channel entry ($T_{w,min,1}$ = 1257.2 K, slightly above the theoretical minimum value of 1256.7 K from Eq. (1) calculated using Le_{CO} = 1.06). Farther downstream, $T_{w,1}$ increases and would have eventually reached the adiabatic equilibrium temperature T_{ad} = 1292.9 K upon complete conversion of CO, which however does not occur for the 30-mm channel length.

For Case 2, with a detailed catalytic reaction mechanism and heat conduction in the solid (Figures 4b and 4b1), the finite-rate chemistry further decreases the wall temperature to 1236.4 K at the channel entry, which is 20.8 K lower than that of Case 1 and 56.5 K lower than T_{ad}. Cases 1 and 2 result in slightly different conversions of CO at the channel exit (52.0% for Case 1 and 51.3% for Case 2, see Figure 4b1). Gas-phase combustion is not ignited, since the gas-phase oxidation of CO requires H-containing species to be initiated at realistic temperatures (Glassman et al., 2014). Therefore, the simulations of Case 3 with both surface and gaseous chemistry coincide with those of Case 2 and are not shown in Figures 4b and 4b1.

4.1.3. CH₄/air catalytic combustion

Methane is shown in Figures 4c and 4c1 for two equivalence ratios. Simulations are first given for a CH_4/air mixture at φ = 0.3 (same φ as for the H_2 and CO fuels discussed

before). For Case 1, with infinitely fast chemistry and no solid heat conduction, the slightly lower than unity methane Lewis number (Le_{CH4} = 0.97) leads to a maximum wall temperature $T_{w,max,1}$ = 1082.0 K at the channel entry, which is 15.1 K higher than T_{ad} and is in good agreement with the value calculated using Eq. (1): 1082.2 K. The wall temperature $T_{w,1}$ drops mildly with increasing streamwise distance, while the CH_4 conversion at the channel exit reaches 52.6%.

Considering the much lower volumetric composition of CH_4 (3.05%) than H_2 and CO (11.2%) at the same equivalence ratio φ = 0.3, the resulting heat release for CH_4 is considerably lower (T_{ad} = 1066.9 K compared to 1189.4 K and 1292.9 K for H_2 and CO, respectively). Thus, simulation of CH_4 with a higher φ = 0.4 (vol. 4.04%) is also included. Although the volumetric content of CH_4 is still lower than that of the other two fuels, its corresponding adiabatic equilibrium temperature T_{ad} = 1282.2 K is already higher than that of H_2 and very close to CO. This is a result of the much higher volumetric exothermicity of methane: 800 kJ/mol for CH_4 versus 240 kJ/mol for H_2 and 282 kJ/mol for CO. Increasing φ from 0.3 to 0.4 also leads to higher mean gas temperatures (712.5 K and 853.4 K, respectively, at the channel exit) and higher methane conversions (52.6% and 55.0%, respectively).

For the present inlet conditions (T_{IN} = 300 K, p = 1 bar), catalytic or gas-phase combustion of methane cannot be ignited under finite-rate chemistry. Our previous studies (Carroni et al., 2003; Reinke et al., 2002) have shown that fuel-lean CH_4/air mixtures at atmospheric pressure need preheating to at least 600 K in order to sustain catalytic combustion. Therefore, the corresponding Cases 2 (detailed surface chemistry) and 3 (detailed surface and gaseous chemistry) are not shown in Figures 4c and 4c1 as they do not lead to ignited solutions.

In summary, the infinitely fast catalytic chemistry simulations $T_{w,1}$ in Figure 4 indicate that the high diffusivity (or low Le) of H_2 is beneficial when high external heat transfer is required. Despite the lowest volumetric heat release rate of H_2 compared to CO and CH_4, its high molecular transport leads to the highest (superadiabatic) surface temperatures, albeit with a large spatial non-uniformity. The almost diffusionally neutral ($Le \sim 1$) CH_4 fuel yields much more spatially uniform wall temperatures $T_{w,1}$ and, given its highest volumetric heat release rate, it can attain high surface temperatures at lower volumetric contents. For CO, however, its lowest diffusivity and its intermediate volumetric heat release rate yield the least attractive performance, with moderately under-adiabatic surface temperatures $T_{w,1}$ over the entire channel length and lowest conversions. When realistic catalytic chemistry is introduced ($T_{w,2}$ simulations) the advantages of methane are largely removed, since its lowest reactivity necessitates high inlet temperatures to achieve ignition and this may not be feasible in many practical systems. Finite-rate chemistry improves the combustion characteristics of H_2 by moderating the peak wall temperature at the channel entry (compare $T_{w,1}$ and $T_{w,2}$ in Figure 4a), while it deteriorates the performance of CO by reducing the wall temperatures to even lower under-adiabatic values. Thus, the interplay of thermodynamics (heat release rate), transport (Lewis number), and chemistry (reactivity) is very rich and has to be considered when designing catalytic microreactors.

4.2. *Impact of gas-phase reactions and selection of channel diameter*

As discussed in Figure 4a, the presence of gaseous combustion leads to decreased wall temperatures and to increased temperature spatial non-uniformity. Moreover, gaseous combustion is detrimental as it increases the energy losses due to the higher temperature

of the exhaust gases (compare $T_{\text{gas-m,3}}$ and $T_{\text{gas-m,2}}$ in Figure 4a). For a given inlet temperature and equivalence ratio, gas-phase combustion is primarily controlled by the wall temperature and the surface-to-volume ratio. Additional 2D channel simulations are shown below, delineating the operating and geometrical parameters where gaseous combustion is suppressed.

The computed contribution of gaseous chemistry to the total fuel conversion (catalytic and gaseous) in a Pt-coated cylindrical channel with a length of 30 mm, is plotted in Figure 5 as a function of the channel diameter for H_2/CO/air and H_2/CH_4/air mixtures with a global $\varphi = 0.3$ (based on both fuel components), $T_{\text{IN}} = 300$ K, $U_{\text{IN}} = 30$ m/s, and $p = 1$ bar. Detailed surface and gaseous chemical reaction mechanisms (described in section 3.1) are used. The H_2/CO/air mixture in Figure 5a corresponds to Case A1 in Table 1, while the H_2/CH_4/air mixture in Figure 5b corresponds to Case B1. The channel wall temperatures are kept constant at 1600 K, 1450 K, and 1296 K (Figure 5a) or 1258 K (Figure 5b). The lowest temperatures refer to the highest measured surface temperatures in groups A and B of Table 1, respectively.

Figure 5a illustrates that, for the H_2/CO/air mixture and for the 1.5-mm diameter of the microreactor channels (Figure 1), the contribution of gaseous H_2 conversion at 1296 K is 0.08% and that of CO is 0.13%. For the H_2/CH_4/air mixture in Figure 5b, the gaseous conversion contributions of H_2 and CH_4 at 1258 K are 0.05% and 0.67%, respectively. Considering that 1296 K in Figure 5a and 1258 K in Figure 5b refer to the maximum attained surface temperatures in the ensuing experiments, the actual gaseous conversions should be even lower. Consequently, the selected 1.5 mm channel diameter safely ensures suppression of the detrimental gaseous combustion during microreactor operation.
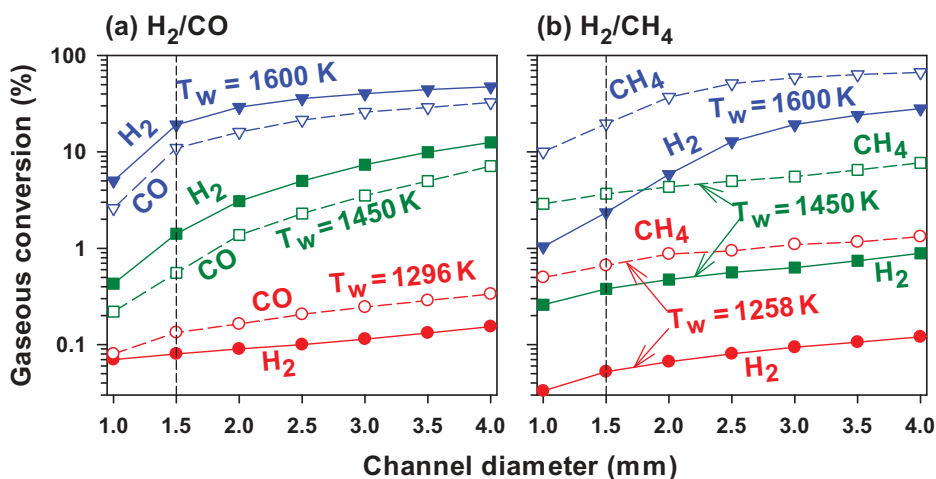

Figure 5. Computed contribution of gaseous chemistry to the total fuel conversion (catalytic and gaseous) in a Pt-coated cylindrical channel with a length of 30 mm, as a function of channel diameter. Fuel/air catalytic combustion with $\varphi = 0.3$, $T_{\text{IN}} = 300$ K, $U_{\text{IN}} = 30$ m/s, $p = 1$ bar. (a) H_2 (solid lines) and CO (dashed lines) for a mixture with H_2:CO ratio 9 (Case A1 in Table 1); (b) H_2 (solid lines) and CH_4 (dashed lines) for a mixture with H_2:CH_4 ratio 9 (Case B1 in Table 1). The channel surface temperatures are prescribed at 1600 K (triangles), 1450 K (squares), and maximum values (circles) attained in the experiments of each case (1296 K for H_2/CO and 1258 K for H_2/CH_4).

4.3. *Comparison of temperature measurements and predictions*

The experimental cases in Table 1 are divided into three groups: Cases A1–A9 refer to H_2/CO/air mixtures, while Cases B1–B9 and C1–C9 to H_2/CH_4/air mixtures. Cases in Group B have $CH_4:H_2$ vol. ratios, which are the same as the $CO:H_2$ vol. ratios, and also the same global φ as the corresponding cases in Group A. Cases in Group C have the same volumetric composition of H_2 and the same adiabatic equilibrium temperature T_{ad} (i.e., practically the same inlet chemical power) as the corresponding cases in Group A; this implies an adjusted amount of CH_4 and slightly different global φ, compared to the Group B cases.

Similar to our earlier study on H_2/air combustion (Sui et al., 2016), two different configurations are studied: coflow and counterflow. The counterflow arrangement is achieved by exchanging the connections of the supply and exhaust Teflon tubes that are attached to the 2-mm ID and 100-mm-long 12 steel connecting tubes shown in Figure 1b. Flow directions in the channels are depicted with arrows in Figures 6a2 and 6b2. It was shown in our earlier work that the counterflow arrangement yields the best temperature uniformity of the upper microreactor surface, which is optimal for power generation coupled with thermophotovoltaic (TPV) devices. Hence, the main focus is on the counterflow arrangement, while coflow is only shown briefly for comparison purposes.

Photographs of the reactor upper surface taken with a conventional camera and simulated 2D temperature distributions for the coflow and counterflow in Case A5 are shown in Figure 6. The yellow-red colors in the photographs indicate high temperatures and the simulations show qualitative agreement with the photograph patterns. As shown in Figure 6, for the coflow configuration, the temperature is highest in the upstream
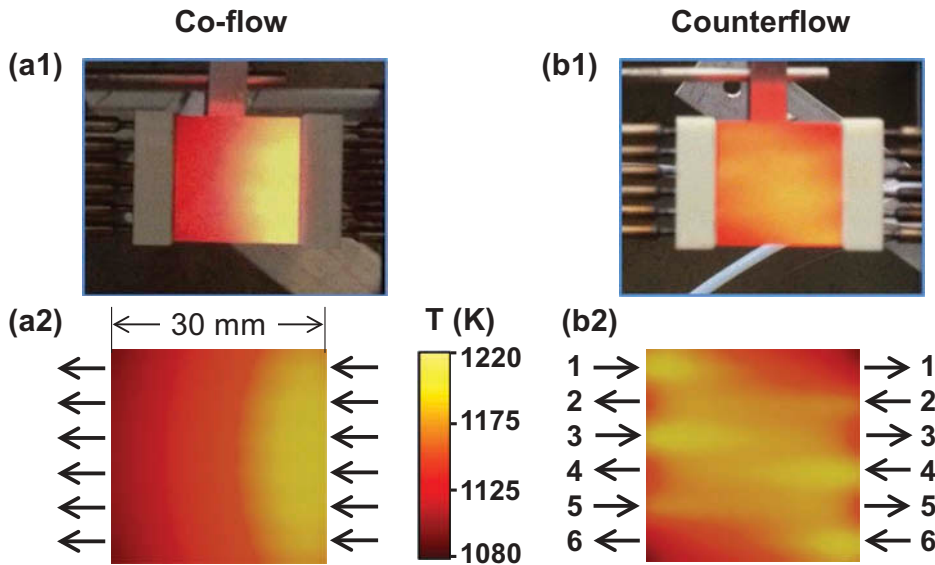

Figure 6. Photographs (a1), (b1) and simulations (a2), (b2) of upper surface temperature distributions for the coflow and counterflow configurations for Case A5 (vol. ratio $CO:H_2 = 1:9$, $\varphi = 0.4$, and $U_{IN} = 50$ m/s).

section and decreases gradually downstream. This is in agreement with the temperature profiles of the single channel H_2 simulations in Figure 4a. On the other hand, for the counterflow configuration in Figures 6b1 and 6b2, better surface temperature uniformity is achieved. The qualitative agreement of the 2D spatial patterns in Figure 6 allows for the subsequent quantification of the agreement between measurements and predictions by comparing temperature Probability density function (PDF) shapes and first and second moments.

Comparisons between measured (using the IR camera) and predicted temperature PDFs of the upper microreactor surface are shown in Figure 7 for Cases A1–A3. Coflow leads to broader and nearly bimodal PDFs, while counterflow yields narrower and more symmetric PDFs. As φ is increased, all PDFs become broader. Measured and predicted mean values, standard deviations, and distribution shapes in Figure 7 are in good agreement with each other, as shown in Table 2. Comparisons of PDFs for fixed φ and varying U_{IN} yield qualitatively the same agreement and are not shown here. In the following, only the counterflow configuration is discussed.
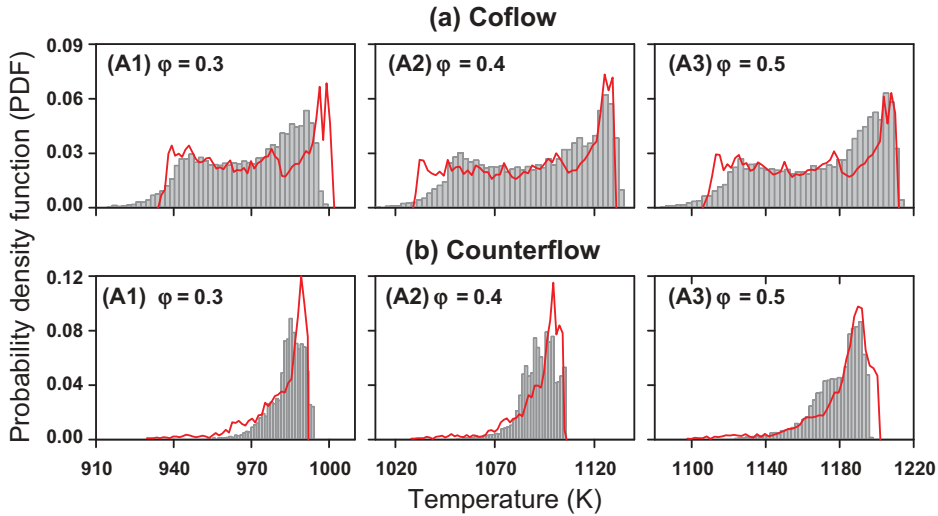
Figure 7. Measured (gray areas) and predicted (solid lines) temperature PDFs of the upper reactor surface for Cases A1-A3 (CO:H_2 = 1:9; U_{IN} = 30 m/s; φ = 0.3, 0.4, and 0.5) in Table 1: (a) coflow and (b) counterflow configuration. Measured and predicted mean temperatures T_{mean} and temperature standard deviations σ_T are further given in Table 2.

Table 2. Comparison between measured and predicted mean values and standard deviations of temperature for the cases in Figure 7.

| Case	Mean temperature T_{mean} (K)		Standard deviation σ_T (K)	
	Measured	Predicted	Measured	Predicted
A1-coflow	967	971	18.9	20.3
A1-counterflow	979	981	10.6	11.3
A2-coflow	1086	1085	29.4	31.1
A2-counterflow	1093	1091	13.3	13.4
A3-coflow	1172	1165	32.2	32.9
A3-counterflow	1176	1182	15.6	17.4

4.4. Measurements and simulations of H_2/CO and H_2/CH_4 fuel combustion

Measured and predicted maximum, minimum, and mean upper surface temperatures for the H_2/CO/air Cases A1–A9 are plotted versus equivalence ratio in Figure 8. These cases are divided into three subgroups: Cases A1–A3 (U_{IN} = 30 m/s, CO:H_2 = 1:9), Cases A4–A6 (U_{IN} = 50 m/s, CO:H_2 = 1:9), and Cases A7–A9 (U_{IN} = 30 m/s, CO:H_2 = 2:8). Measured and predicted exhaust gas compositions for the same cases are shown in Figure 9, where all measurements have been converted from dry to wet basis. This is achieved by carrying out balances for the C, H, and O elements. Two linearly independent element conservation equations are constructed, leading to two independent wet compositions (see also Schneider et al., 2006). The small relative deviation (less than 5%) of the two independently assessed wet compositions attests the accuracy of the measurements. The differences between measured and predicted surface temperatures in Figure 8 range from 0.8 K to 24.4 K, while the maximum relative differences between measured and predicted exhaust gas compositions are 6.6% for H_2, 4.9% for CO, 4.1% for O_2, 0.7% for N_2, and 11.8% for CO_2.

The fuel conversions (averaged over the six outlets) for Cases A1–A9 are plotted in Figures 10a1 and 10a2). The H_2 and CO conversions do not exceed 70% and 37%, respectively. However, complete fuel conversion at the reactor outlet is not necessary in the present application, as many microreactors of the type in Figure 1a will be eventually clustered in a recuperative way. The highest measured mean surface temperature in Figure 8 is attained in Case A6 with $T_{mean,max}$ = 1261 K, while the highest difference between maximum and minimum temperatures is ΔT = 132 K. In comparison, the corresponding measurements with only H_2 fuel and the same φ and U_{IN} (Sui et al., 2016) yielded $T_{mean,max}$ = 1277 K and ΔT = 119 K. Finally, the difference between the maximum wall temperatures and the corresponding adiabatic equilibrium temperatures increases with increasing equivalence ratio (see Figure 8a) due to the enhanced radiation heat losses at higher wall temperatures.
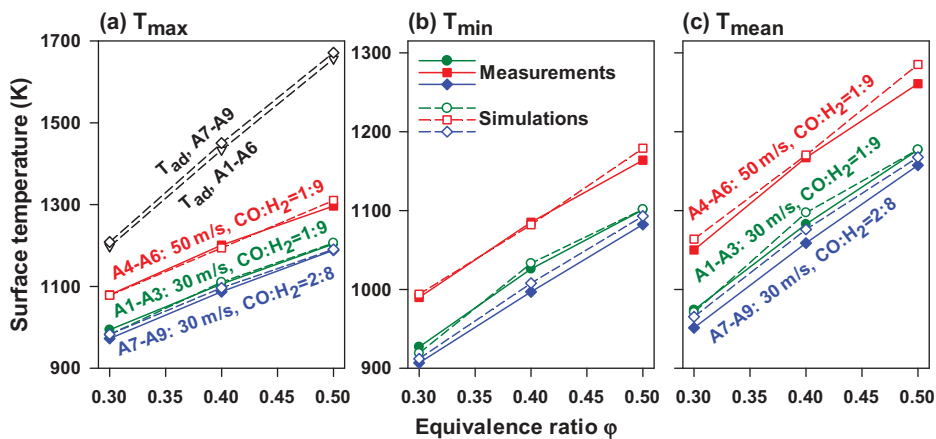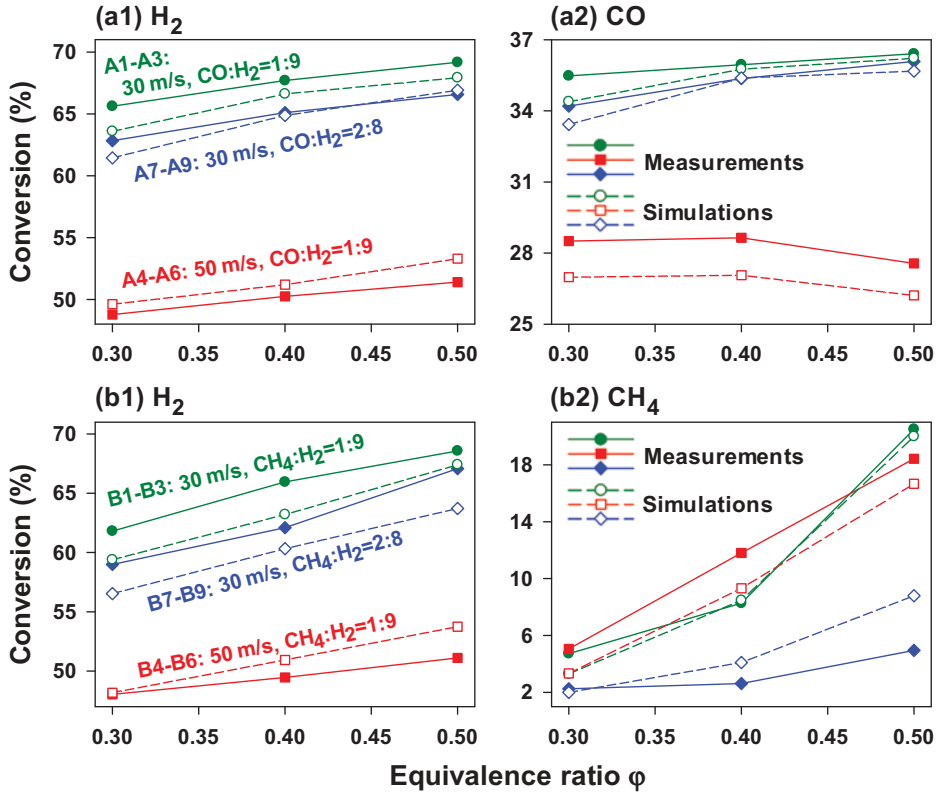

Figure 8. Measured (solid lines and filled symbols) and simulated (dashed lines and open symbols) maximum (a), minimum (b), and mean (c) values of the upper surface temperatures for H_2/CO/air mixtures as a function of the equivalence ratio. The lines marked T_{ad} in (a) denote the adiabatic equilibrium temperatures of the inlet mixtures. CO:H_2 = 1:9, U_{IN} = 30 m/s (circles, Cases A1-A3); CO:H_2 = 1:9, U_{IN} = 50 m/s (squares, Cases A4–A6); and CO:H_2 = 2:8, U_{IN} = 30 m/s (diamonds, Cases A7-A9).
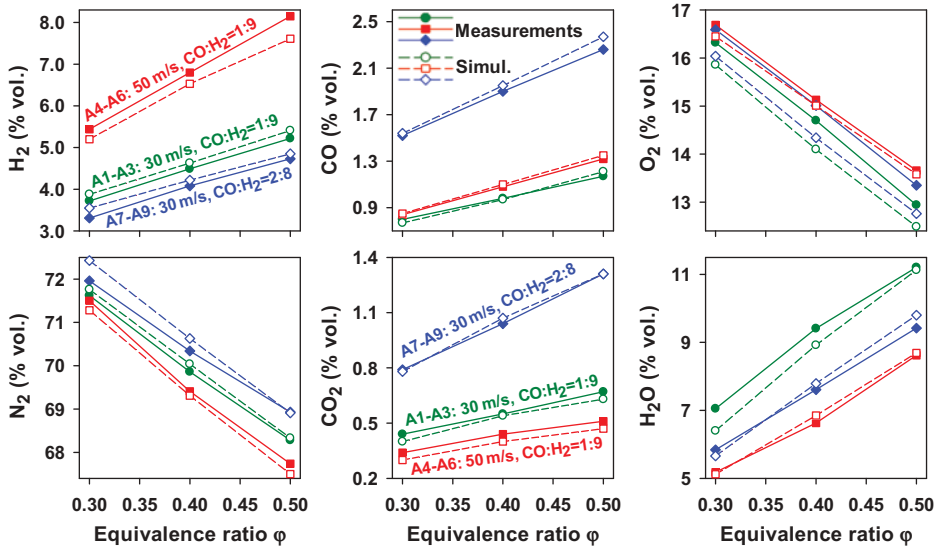
Figure 9. Measured (solid lines and filled symbols) and simulated (dashed lines and open symbols) exhaust species compositions of $H_2/CO/air$ mixtures as a function of the equivalence ratio. $CO:H_2 = 1:9$, $U_{IN} = 30$ m/s (circles, Cases A1-A3); $CO:H_2 = 1:9$, $U_{IN} = 50$ m/s (squares, Cases A4-A6); and $CO:H_2 = 2:8$, $U_{IN} = 30$ m/s (diamonds, Cases A7-A9).

Temperatures increase by nearly 100 K as the inlet velocity is raised from 30 m/s to 50 m/s (Figure 8a), due to the enhanced mass throughput and the resulting increased heat release rate. An additional factor for the increasing temperatures with rising velocities is the high catalytic reactivity of H_2 on Pt, which is maintained even at the very high inflow velocity of 50 m/s. The catalytic reactivity, or equivalently the departure from the infinitely-fast chemistry (transport-limited) fuel conversion, can be examined with the aid of the computed mass fraction radial profiles and the corresponding wall-to-centerline mass fraction ratios in Figures 11A1a–11A1c, 11A6a–11A6c for Cases A1 and A6 with $H_2/$ CO fuels. The simulations refer to channel No. 2 in Figure 6b2; however, similar results are obtained for all six channels. The wall-to-centerline mass fraction ratio of the deficient fuel reactants is a direct measure of the catalytic reactivity: it is identically zero for infinitely-fast chemistry while it is unity for vanishing catalytic reactivity.

Figure 11A1c indicates that the wall-to-centerline mass fraction ratios of H_2 drop to less than 10% for $x > 5$ mm, implying a mixed kinetic/transport controlled H_2 conversion but still heavily weighted towards transport-controlled conversion. Similarly, a high reactivity of CO is evidenced by the low wall-to-centerline ratios in Figure 11A1c that drop to less than ~2% at $x > 2$ mm, values well below the corresponding ones for H_2. The lower ratios for CO may appear surprising as they suggest higher catalytic reactivity for CO compared to H_2. However, this need not be the case since the diffusivity of H_2 is about three times higher than that of CO, such that the surface reactions have to cope with an increased radial transport in the case of H_2. Moreover, the high surface temperatures obtained in the H_2/CO mixture of Case A1 are largely due to H_2 reactions and CO reactions benefit from the exothermicity of hydrogen (characteristically, if H_2 is replaced by CO in Case A1, the predicted maximum surface temperature drops by 393 K). The

Figure 10. Measured (solid lines and filled symbols) and simulated (dashed lines and open symbols) fuel conversions of $H_2/CO/air$ (a1), (a2) and $H_2/CH_4/air$ (b1), (b2) mixtures as a function of the equivalence ratio. Symbol notation as in Figures 8 and 9.

much higher transport of H_2 is also seen by comparing Figures 11A1a and 11A1b; the radial depletion of H_2 is strong at the channel centerline ($r = 0$), whereas the CO mass fraction at the centerline remains unaltered even at $x = 30$ mm. For the higher velocity and equivalence ratio Case A6, Figures 11A6a–11A6c indicate increased finite rate chemistry effects for both H_2 and CO. Moreover, a slower chemistry of CO compared to H_2 is seen in Figure 11A6c for $x < 12$ mm, as manifested by the higher wall-to-centerline CO mass fraction ratios.

Comparison of Cases A1–A3 with Cases A7–A9 in Figure 8 shows that an increase of the volumetric CO:H_2 ratio from 1:9 to 2:8 leads to about 20 K lower temperatures. This happens despite the larger heat of combustion of CO per volume (282 kJ/mol) compared to H_2 (240 kJ/mol) and comes as a result of the higher transport and higher reactivity of H_2 and the resulting Lewis number induced high surface temperatures. The lower wall temperatures and lower reactivity with increasing amount of CO in the inlet mixture, leads to higher CO and product CO_2 in the exhaust (see Figure 9) in spite of the reduced conversion of CO (see Figure 10a2). Similarly, H_2 has a lower conversion when it is partly replaced with CO (Figure 10a1).

Measured and predicted maximum, minimum, and mean upper surface temperatures of the $H_2/CH_4/air$ Cases B1–B9 (with same global φ and CH_4:H_2 vol. ratios as Cases A1–A9)

are plotted in Figure 12. Similar to the H_2/CO/air mixtures, cases are divided into three subgroups: Cases B1–B3 (U_{IN} = 30 m/s, CH_4:H_2 = 1:9), Cases B4–B6 (U_{IN} = 50 m/s, CH_4:H_2 = 1:9), and Cases B7–B9 (U_{IN} = 30 m/s, CH_4:H_2 = 2:8). The exhaust compositions are shown in Figure 13 and the fuel conversions in Figures 10b1 and 10b2. Radial profiles of H_2 and CH_4 mass fractions and wall-to-centerline mass fraction ratios are plotted for Cases B1 and B6 in Figures 11B1a–11B1c and 11B6a–11B6c. The highest measured mean temperature is attained in Case B6 (1229 K, Figure 12a). An increase of inlet velocity from 30 m/s to 50 m/s with fixed compositions yields ~80 K higher surface temperature, and a larger H_2 slip in the exhaust (Figure 13a).
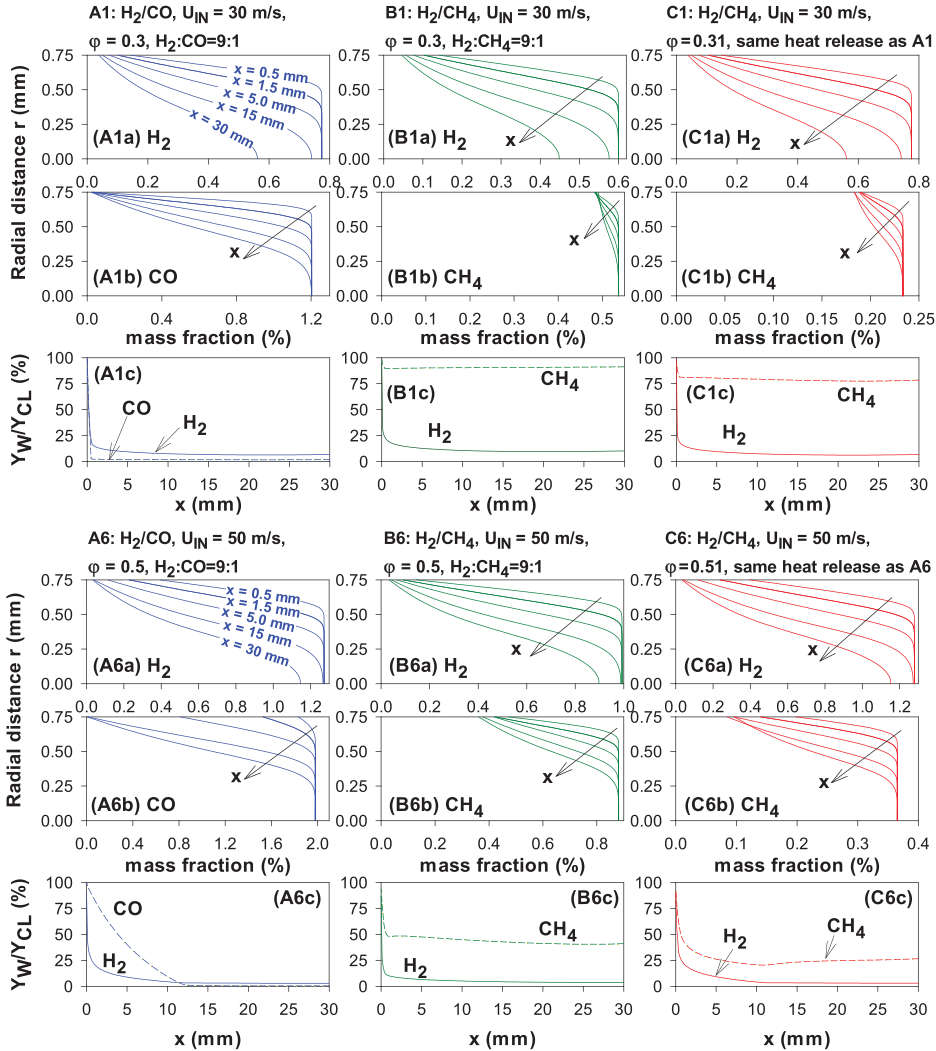
Figure 11. Predicted radial profiles (r = 0 is the channel centerline and r = 0.75 mm the gas-wall interface) of fuel mass fractions and wall-to-centerline ratios of fuel mass fractions in one catalytic channel of the reactor, at five selected axial positions (x = 0.5 mm, 1.5 mm, 5 mm, 15 mm, and 30 mm) for Cases A1, B1, C1, A6, B6, and C6. Mass fraction plots are denoted by the suffixes "a" or "b" appended to the case name, while the suffix "c" denotes wall-to-centerline mass fraction ratios.
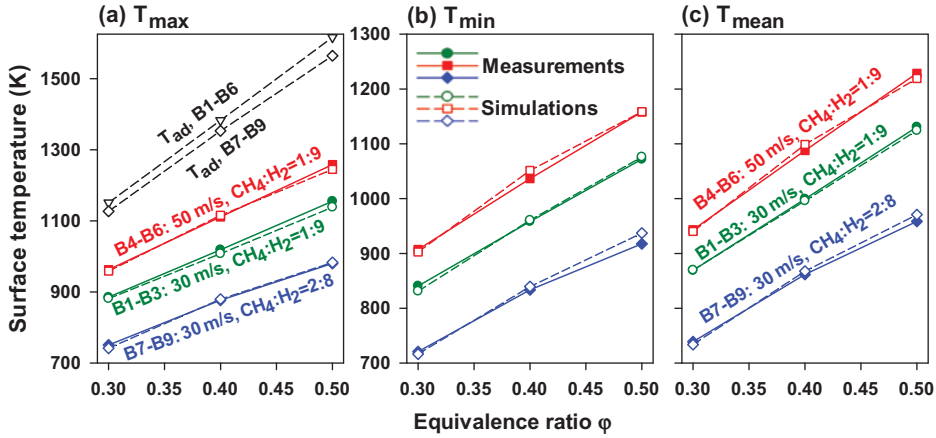
Figure 12. Measured (solid lines and filled symbols) and simulated (dashed lines and open symbols) maximum, minimum, and mean values of the top surface temperatures of $H_2/CH_4/$air mixtures as a function of the equivalence ratio for $CH_4{:}H_2 = 1{:}9$, $U_{IN} = 30$ m/s (circles, Cases B1-B3); $CH_4{:}H_2 = 1{:}9$, $U_{IN} = 50$ m/s (squares, Cases B4-B6); and $CH_4{:}H_2 = 2{:}8$, $U_{IN} = 30$ m/s (diamonds, Cases B7-B9).
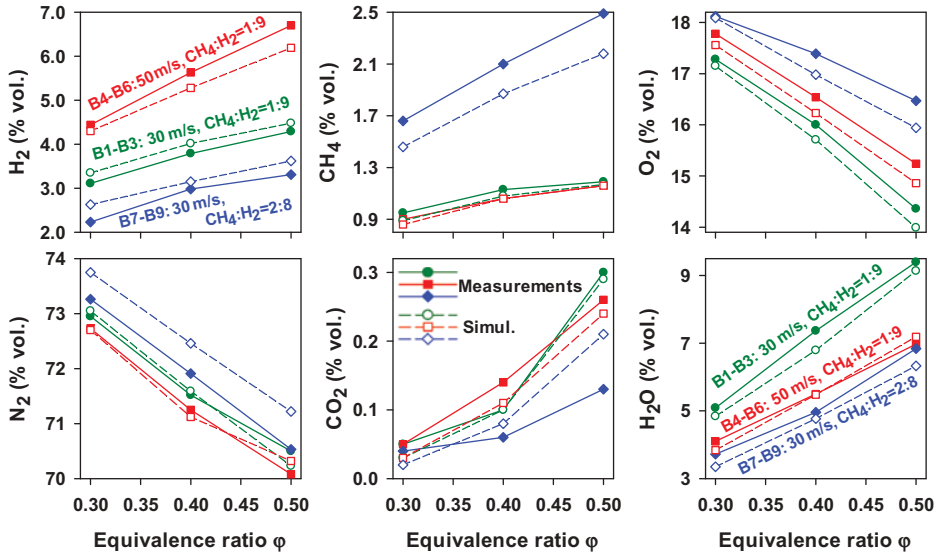
Figure 13. Measured (solid lines and filled symbols) and simulated (dashed lines and open symbols) exhaust species compositions of $H_2/CH_4/$air mixtures as a function of the equivalence ratio for $CH_4{:}H_2 = 1{:}9$, $U_{IN} = 30$ m/s (circles, Cases B1-B3); $CH_4{:}H_2 = 1{:}9$, $U_{IN} = 50$ m/s (squares, Cases B4-B6); and $CH_4{:}H_2 = 2{:}8$, $U_{IN} = 30$ m/s (diamonds, Cases B7-B9).

Partial substitute of H_2 by CH_4 (increase of $CH_4{:}H_2$ ratio from 1:9 to 2:8) leads to a drop in surface temperatures by more than 150 K in all investigated cases (Figure 12). The much higher exothermicity (800 kJ/mol) of CH_4 does not compensate for its low surface reactivity. The very low CH_4 reactivity is clearly evident in the transverse CH_4 profiles and

the high wall-to-centerline CH_4 mass fraction ratios in Figure 11 for Cases B1, B6, C1, and C6.

## 4.5. Comparisons of CO and CH₄ combustion with H₂

Direct comparison of CO and CH_4 fuels is discussed in Figure 14. Maximum and mean temperatures as well as H_2/CO/CH_4 conversions are plotted as functions of equivalence ratio. Three groups are compared: Cases A4–A6 with CO:H_2 ratio 1:9, Cases B4–B6 with CH_4:H_2 ratio 1:9 and same global φ as Cases A4–A6, and finally Cases C4–C6 with CH_4/H_2 mixtures having the same volumetric fraction of H_2 and same T_{ad} (i.e., roughly the same chemical input power) as the corresponding Cases A4–A6.

Inspection of the surface temperatures in Figure 14 reveals that CO is superior to CH_4. Despite the lower exothermicity and larger Lewis number of CO than CH_4, Group A has consistently higher surface temperatures. This is due to the faster catalytic chemistry of CO compared to CH_4, as shown previously by the wall-to-centerline CO and CH_4 mass fraction ratios in Figure 11 (A6, B6, and C6). Comparisons of predicted upper surface temperature distributions for Cases A4, B4, C4 and of the corresponding case with only H_2 fuel from Sui et al. (2016) are shown in Figure 15. It is seen that the addition of CO or CH_4 in H_2 (either by keeping the same
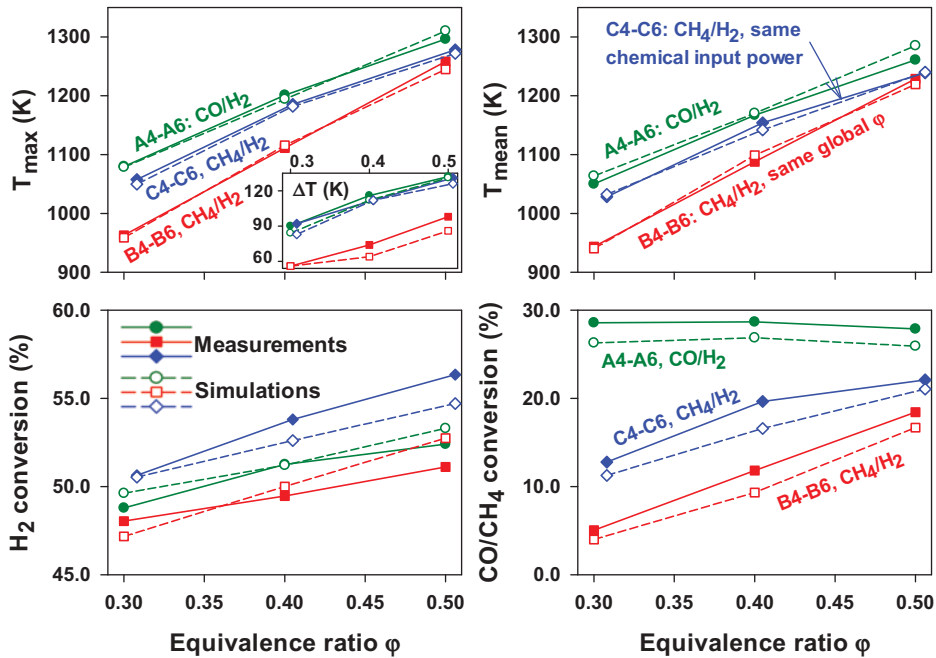
Figure 14. Measured (solid lines and filled symbols) and predicted (dashed lines and open symbols) maximum, mean, and difference ΔT between maximum and minimum surface temperatures, and fuel conversions for U_{IN} = 50 m/s as a function of equivalence ratio φ for: H_2/CO mixtures (CO:H_2 = 1:9, circles, Cases A4-A6); H_2/CH_4 mixtures with same H_2/CH_4 ratio and same global φ as Cases A (squares, Cases B4-B6); and H_2/CH_4 mixtures with same inlet vol. fractions of H_2 and same exothermicity as Cases A (diamonds, Cases C4-C6).
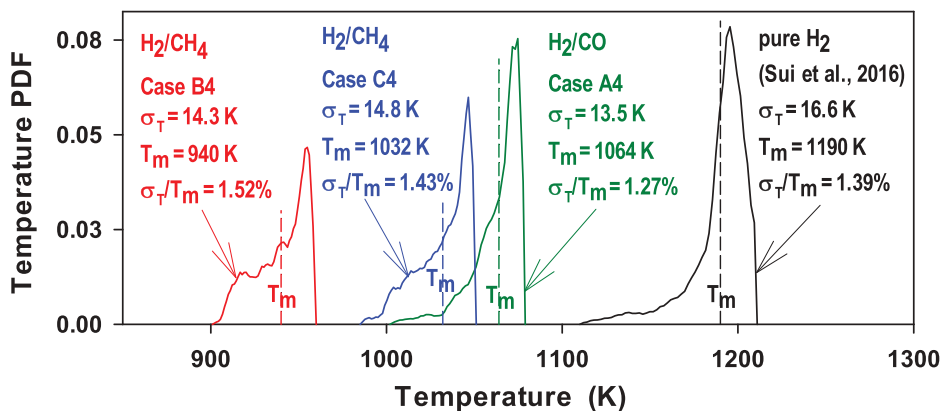
Figure 15. Predicted temperature probability density functions for U_{IN} = 50 m/s. Cases A4 (φ = 0.3, CO: H_2 = 1:9), B4 (φ = 0.3, CH_4:H_2 = 1:9), and C4 (φ = 0.31, CH_4:H_2 = 0.36:9.64, same exothermicity as Case A4). Undiluted H_2 (φ = 0.3) from Sui et al., (2016) is also shown.

equivalence ratio for CO and CH_4 or by keeping the same exothermicity for CH_4) reduces the mean temperature. On the other hand, the temperature standard deviations σ_T and especially the normalized ratios σ_T/T are roughly the same for all cases in Figure 15. The total radiated power $P = \int_A \varepsilon(T)\sigma T^4 dA$ (where $\varepsilon(T)$ is calculated from Figure 3, σ is the Stefan–Boltzmann constant, and the integral is carried out over the upper surface area A = 30 × 30 mm^2) is greatly reduced in the sequence H_2, H_2/CO, and H_2/CH_4 fuel mixtures and, moreover, the normalized standard deviations of the radiated power increase. The total radiated powers for the pure H_2 and for Cases A4, C4, and B4 in Figure 15 are P = 70.5 W, 43.7 W, 38.1 W, and 25.5 W, respectively, while the corresponding relative standard deviations σ_p/P are 5.3%, 5.4%, 6.0%, and 6.5%.

In summary, H_2 is the most suitable fuel for microreactors operating at very lean stoichiometries in air ($\varphi \leq 0.5$) and requiring high surface temperatures. The intrinsic large surface temperature non-uniformity (see Figure 4a) of H_2 can be overcome with appropriate reactor design optimizations, e.g., the multi-channel counterflow configuration in Figure 1. Syngases and biogases (mainly CO/H_2 mixtures) provide lower wall temperatures even for small overall volumetric ratios CO:H_2 (1:9 and 2:8); although the reactivity of CO is typically high, its larger than unity Lewis numbers hinder the attainment of high wall temperatures. Mixtures of H_2/CH_4 (e.g., fuels produced by decarbonization of natural gas) yield the lowest wall temperatures and, hence, are the least attractive due to the substantially lower catalytic reactivity of CH_4. It is nevertheless envisaged that for higher equivalence ratios ($\varphi > 0.5$), which are outside the scope of the present work, CH_4/H_2 mixtures can still provide acceptably high temperatures.

5. Conclusions

The catalytic combustion of fuel-lean H_2/CO/air and H_2/CH_4/air mixtures was investigated in a 30 × 30 × 4 mm^3 ceramic (SiC) microreactor equipped with six 1.5-mm-ID platinum tubes. The goal was to demonstrate high surface temperatures (>1200 K) with

good spatial uniformity for power generation applications in conjunction with TPV units. Various fuel compositions, fuel-lean stoichiometries, and mass throughputs were studied. The upper surface temperatures of the microreactor were assessed with an IR camera and the exhaust gas composition was monitored with a micro-GC. 3D simulations with detailed catalytic and gas-phase chemistry, conjugate heat transfer, and external heat losses were employed. The following are the key conclusions of this study:

(1) The combustion characteristics of H_2, CO, and CH_4 over Pt were very diverse due to the disparately different thermodynamic (heat release), transport (Lewis number), and kinetic reactivity) properties of the three fuels. Catalytic combustion of CH_4 and especially of H_2 at lean stoichiometries in air could lead to superadiabatic surface temperatures due to the less than unity Lewis number of the deficient fuel (Lewis numbers $Le_{H2} \sim 0.35$ and $Le_{CH4} \sim 0.97$); this behavior was highly desirable for microreactors operating with high external heat losses. On the other hand, the slightly larger than unity Lewis number of CO ($Le_{CO} \sim 1.06$ at lean stoichiometries in air) resulted in moderately underadiabatic surface temperatures.

(2) The presence of gaseous combustion lowered the catalyst temperatures and increased the exhaust gas temperatures, and was thus detrimental for applications with a desired high external surface heat transfer. Gaseous combustion could be effectively suppressed by proper selection of the catalytic channel geometrical confinement (diameter).

(3) Hydrogen exhibited the largest temperature spatial non-uniformity in catalytic channel-flow combustion among the three investigated fuels, which was a result of its low Lewis number. However, microreactor design optimizations (multiple channels with opposed flow directions) could ensure good spatial temperature uniformities for H_2/air catalytic combustion with standard deviations less than 20 K. Methane had the lowest reactivity on Pt and did not ignite catalytically at atmospheric pressure without a substantial preheat.

(4) Measured maximum surface temperatures of H_2/CO and H_2/CH_4 fuel blends increased with rising mass throughput (inlet velocity), equivalence ratio, and hydrogen volumetric content. For a H_2/CO/air mixture with U_{IN} = 50 m/s, φ = 0.50, and CO:H_2 ratio 1:9, the maximum attained mean surface temperature was 1261 K, with a standard deviation of 18.3 K. For a H_2/CH_4/air mixture with U_{IN} = 50 m/s, φ = 0.50, and CH_4:H_2 ratio 1:9, the maximum mean surface temperature was 1229 K, with a standard deviation of 14.6 K. In comparison, the corresponding measurements with only H_2 fuel were 1277 K and 18.9 K.

(5) Comparisons between measurements and predictions were very favorable in terms of mean values, standard deviations, and PDF shapes of temperature. Characteristically, mean temperatures differed by 0.6–14.4 K and standard deviations by 0.1–3.2 K. Moreover, measured and predicted exhaust compositions had relative differences 0.5–6.5% for H_2, CH_4, and CO, and 1.8–11.8% for CO_2. Mean surface temperatures dropped when replacing H_2 volumetrically with CO. This drop was even greater in H_2/CH_4 mixtures when either the equivalence ratio or the exothermicity was kept the same as the corresponding H_2/CO mixtures. Normalized temperature standard deviations σ_T/T remained largely unaffected for H_2, H_2/CO, or H_2/CH_4 fuel mixtures (1.27–1.52%). However, the normalized

standard deviation of the radiated power increased for the H_2/CO and H_2/CH_4 mixtures by as much as 22% compared to the only H_2 fuel.

(6) The fuel of choice for microreactors requiring high surface temperatures and operating at very lean stoichiometries in air ($\varphi \leq 0.5$) was H_2. Syngas or biogas (H_2/CO mixtures) yielded lower wall temperatures compared to undiluted H_2, even for small volumetric $CO:H_2$ ratios (1:9 and 2:8). Although the reactivity of CO was typically high when combusting in H_2/CO mixtures, its larger than unity Lewis number did not allow for the attainment of high wall temperatures. Mixtures of H_2/CH_4 (such as fuels formed by decarbonization of natural gas) were the least attractive at lean stoichiometries in air due to the significantly lower catalytic reactivity of CH_4 that led to the lowest wall temperatures.

Acknowledgments

Nomenclature

Le_k Lewis number of kth species (thermal over mass diffusivity)
R catalytic channel radius
T_{ad} adiabatic equilibrium temperature
T_{IN} inlet temperature
U_{IN} inlet streamwise velocity
x, r streamwise and radial coordinates of catalytic channels

Greek symbols

ε surface emissivity
σ Stefan–Boltzmann constant
σ_T standard deviation of surface temperature
φ fuel-to-air equivalence ratio

Subscripts

IN   inlet
max, mean, min   maximum, mean, and minimum of surface temperature
gas   gas properties
w   wall

ORCID

Ran Sui   http://orcid.org/0000-0003-3758-7506
John Mantzaras   http://orcid.org/000-0002-1039-669X

References

Appel, C., Mantzaras, J., Schaeren, R., Bombach, R., and Inauen, A. 2005. Turbulent catalytically stabilized combustion of hydrogen/air mixtures in entry channel flows. *Combust. Flame*, **140**, 70–92.

Appel, C., Mantzaras, J., Schaeren, R., Bombach, R., Inauen, A., Kaeppeli, B., Hemmerling, B., and Stampanoni, A. 2002. An experimental and numerical investigation of homogeneous ignition in catalytically stabilized combustion of H_2/air mixtures over platinum. *Combust. Flame*, **128**, 340–368.

American Society of Heating, Refrigerating and Air-conditioning Engineers (ASHRAE). 2009. *ASHRAE Handbook of Fundamentals* (SI Edition), ASHRAE, Atlanta, GA.

Bui, P.A., Vlachos, D.G., and Westmoreland, P.R. 1996. Homogeneous ignition of hydrogen/air mixtures over platinum. *Proc. Combust. Inst.*, **26**, 1763–1770.

Carroni, R., Griffin, T., Mantzaras, J., and Reinke, M. 2003. High-pressure experiments and modeling of methane/air catalytic combustion for power generation applications. *Catal. Today*, **83**, 157–170.

Coltrin, M.E., Kee, R.J., and Rupley, F.M. 1996. Surface Chemkin: A Fortran package for analyzing heterogeneous chemical kinetics at the solid surface-gas phase interface. Report No. SAND90-8003C. Sandia National Laboratories, Albuquerque, NM.

Deutschmann, O., Maier, L.I., Riedel, U., Stroemman, A.H., and Dibble, R.W. 2000. Hydrogen assisted catalytic combustion of methane on platinum. *Catal. Today*, **59**, 141–150.

Diehm, C., and Deutschmann, O. 2014. Hydrogen production by catalytic partial oxidation of methane over staged Pd/Rh coated monoliths: Spatially resolved concentration and temperature profiles. *Int. J. Hydrogen Energy*, **39**, 17998–18004.

Eriksson, S., Wolf, M., Schneider, A., Mantzaras, J., Raimondi, F., Boutonnet, M., and Järas, S. 2006. Fuel rich catalytic combustion of methane in zero emissions power generation processes. *Catal. Today*, **117**, 447–453.

Evans, C.J., and Kyritsis, D.C. 2009. Operational regimes of rich methane and propane/oxygen flames in mesoscale non-adiabatic ducts. *Proc. Combust. Inst.*, **32**, 3107–3114.

Federici, J.A., and Vlachos, D.G. 2011. Experimental studies on syngas catalytic combustion on Pt/Al_2O_3 in a microreactor. *Combust. Flame*, **158**, 2540–2543.

Ghermay, Y., Mantzaras, J., and Bombach, R. 2010. Effects of hydrogen preconversion on the homogeneous ignition of fuel-lean H_2/O_2/N_2/CO_2 mixtures over platinum at moderate pressures. *Combust. Flame*, **157**, 1942–1958.

Ghermay, Y., Mantzaras, J., and Bombach, R. 2011a. Experimental and numerical investigation of hetero-/homogeneous combustion of CO/H_2/O_2/N_2 mixtures over platinum at pressures up to 5 bar. *Proc. Combust. Inst.*, **33**, 1827–1835

Ghermay, Y., Mantzaras, J., Bombach, R., and Boulouchos, K. 2011b. Homogeneous combustion of fuel lean H_2/O_2/N_2 mixtures over platinum at elevated pressures and preheats. *Combust. Flame*, **158**, 1491–1506.

Glassman, I., Yetter, R.A., and Glumac, N.G. 2014. *Combustion*, 5th Edition, Academic Press.

Ju, Y.G., and Maruta, K. 2011. Microscale combustion: Technology development and fundamental research. *Prog. Energy Combust. Sci.*, London, **37**, 669–715.

Kaisare, N.S., Lee, J.H., and Fedorov. A.G. 2005. Operability analysis and design of a reverse-flow microreactor for hydrogen generation via methane partial oxidation. *Ind. Eng. Chem. Res.*, **44**, 8323–8333.

Kaisare, N.S., and Vlachos, D.G. 2012. A review on microcombustion: Fundamentals, devices and applications. *Prog. Energy Combust. Sci.*, **38**, 321–359.

Kamijo, T., Suzuki, Y., Kasagi, N., and Okamasa, T. 2009. High-temperature micro catalytic combustor with Pd/nano-porous alumina. *Proc. Combust. Inst.*, **32**, 3019–3026.

Karagiannidis, S., and Mantzaras, J. 2012. Numerical investigation on the hydrogen-assisted start-up of methane-fueled, catalytic microreactors. *Flow Turbul. Combust.*, **89**, 215–230.

Karagiannidis, S., Mantzaras, J., and Boulouchos, K. 2011. Stability of hetero-/homogeneous combustion in propane and methane fueled catalytic microreactors: Channel confinement and molecular transport effects. *Proc. Combust. Inst.*, **33**, 3241–3249.

Kee, R.J., Dixon-Lewis, G., Warnatz, J., Coltrin, M.E., and Miller, J.A. 1996a. A Fortran computer code package for the evaluation of gas-phase multicomponent transport properties. Report No. SAND86–8246. Sandia National Laboratories, Albuquerque, NM.

Kee, R.J., Rupley, F.M., and Miller, J.A. 1996b. Chemkin II: A Fortran chemical kinetics package for the analysis of gas-phase chemical kinetics. Report No. SAND89–8009B. Sandia National Laboratories, Albuquerque, NM.

Kraus, P., and Lindstedt, R.P. 2017. Reaction class-based frameworks for heterogeneous catalytic systems. *Proc. Combust. Inst.*, **36**, 4329–4338.

Kurdyumov, V.N., Pizza, G., Frouzakis, C.E., and Mantzaras, J. 2009. Dynamics of premixed flames in a narrow channel with a step-wise wall temperature. *Combust. Flame*, **156**, 2190–2200.

Kyritsis, D.C., Coriton, B., Faure, F., Roychoudhury, S., and Gomez, A. 2004. Optimization of a catalytic combustor using electrosprayed liquid hydrocarbons for mesoscale power generation. *Combust. Flame*, **139**, 77–89.

Li, J., Zhao, Z., Kazakov, A., Chaos, M., Dryer, F.L., and Scire, J.J. 2007. A comprehensive kinetic mechanism for CO, CH_2O, and CH_3OH combustion. *Int. J. Chem. Kinet.*, **39**(3), 109–136.

Li, Y.H., Chen, G.B., Cheng, T.S., Yeh, Y.L., and Chao, Y.C. 2013. Combustion characteristics of a small-scale combustor with a percolated platinum emitter tube for thermophotovoltaics. *Energy*, **61**, 150–157.

Mantzaras, J. 2014. Catalytic combustion of hydrogen, challenges and opportunities. In A. Dixon (Ed.), *Advances in Chemical Engineering, Vol. 45: Modeling and Simulation of Heterogeneous Catalytic Processes*, Elsevier B.V., New York, pp. 97–157.

Mantzaras, J. 2015. Microscale combustion modeling. In Y. Ju, C. Cadou, and K. Maruta (Eds.), *Microscale Combustion and Power Generation*, Momentum Press LLC, Highland Park, NJ, pp. 69–158.

Norton, D.G., Wetzel, E.D., and Vlachos, D.G. 2004. Fabrication of single-channel catalytic micro-burners: Effect of confinement on the oxidation of hydrogen/air mixtures. *Ind. Eng. Chem. Res.*, **43**, 4833–4840.

OpenFOAM. 2014. The open source CFD toolbox. Available at: www.openfoam.org.

Pizza, G., Frouzakis, C.E., Mantzaras, J., Tomboulides, A.G., and Boulouchos, K. 2010b. Three-dimensional simulations of premixed hydrogen/air flames in microtubes. *J. Fluid Mech.*, **658**, 463–491.

Pizza, G., Mantzaras, J., and Frouzakis, C.E. 2010a. Flame dynamics in catalytic and non-catalytic mesoscale microreactors. *Catal. Today*, **155**, 123–130.

Pizza, G., Mantzaras, J., Frouzakis, C.E., Tomboulides, A.G., and Boulouchos, K. 2009. Suppression of combustion instabilities of premixed hydrogen/air flames in microchannels using heterogeneous reactions. *Proc. Combust. Inst.*, **32**, 3051–3058.

Reinke, M., Mantzaras, J., Schaeren, R., Bombach, R., Kreutner, W., and Inauen, A. 2002. Homogeneous ignition in high-pressure combustion of methane/air over platinum: Comparison of measurements and detailed numerical predictions. *Proc. Combust. Inst.*, **29**, 1021–1029.

Schneider, A., Mantzaras, J., and Jansohn, P. 2006. Experimental and numerical investigation of the catalytic partial oxidation of CH_4/O_2 mixtures diluted with H_2O and CO_2 in a short contact time reactor. *Chem. Eng. Sci.*, **61**, 4634–4649.

Seyed-Reihani, S.A., and Jackson, G.S. 2004. Effectiveness in catalytic washcoats with multi-step mechanisms for catalytic combustion of hydrogen. *Chem. Eng. Sci.*, **59**, 5937–5948.

Stefanidis, G.D., and Vlachos, D.G. 2009. High vs. low temperature reforming for hydrogen production via microtechnology. *Chem. Eng. Sci.*, **64**, 4856–4865.

Sui, R., and Mantzaras, J. 2016. Combustion stability and hetero-/homogeneous chemistry interactions for fuel-lean hydrogen/air mixtures in platinum-coated microchannels. *Combust. Flame*, **173**, 370–386.

Sui, R., Mantzaras, J., and Bombach, R. 2017. A comparative experimental and numerical investigation of the heterogeneous and homogeneous combustion characteristics of fuel-rich methane mixtures over rhodium and platinum. *Proc. Combust. Inst.*, **36**, 4313–4320.

Sui, R., Prasianakis, N.I., Mantzaras, J., Mallya, N., Theile, J., Lagrange, D., and Friess, M. 2016. An experimental and numerical investigation of the combustion and heat transfer characteristics of hydrogen-fueled catalytic microreactors. *Chem. Eng. Sci.*, **141**, 214–230.

Warnatz, J., Dibble, R.W., and Maas, U. 1996. *Combustion, Physical and Chemical Fundamentals, Modeling and Simulation*, Springer-Verlag, New York.

Zheng, X., and Mantzaras, J. 2014. An analytical and numerical investigation of hetero-/homogeneous combustion with deficient reactants having larger than unity Lewis numbers. *Combust. Flame*, **161**, 1911–1922.

Zheng, X., Mantzaras, J., and Bombach, R. 2014. Kinetic interactions between hydrogen and carbon monoxide oxidation over platinum, *Combust. Flame*, **161**, 332–346.